Rearrangement of π-Electron Network and Switching of Edge-Localized π State in Reduced Graphene Oxide

Shintaro Fujii* **and Toshiaki Enoki***

Department of Chemistry, Tokyo Institute of Technology, 2-12-1 Ookayama, Meguro-ku, Tokyo 152-8551, Japan

ABSTRACT Introduced defects can modulate the intrinsic electronic structure of graphene, causing a drastic switch in its electronic and magnetic properties, in which defect-induced localized π states near the Fermi level play an important role. Accordingly, considerable effort has been directed toward detailed characterization of the defect-induced state; however, identification of the chemical nature of the defect-induced state remains a challenge. Here, we demonstrate a method for reliable identification of the localized π states of oxidized vacancy edges in reduced graphene oxide. Depending on the dynamic changes in the oxygen-binding modes, *i.e.*, between carbonyl and ether forms in the vacancy edges, the π-electron network near the edges can rearrange, leading to drastic on−off switching of the localized π state. This switching can be manipulated *via* scanning-probe-induced local mechanical force. This study provides fundamental guidance toward understanding how oxidized defect structures contribute to the unique electronic state of graphene oxide and its potential future applications in electronic devices.

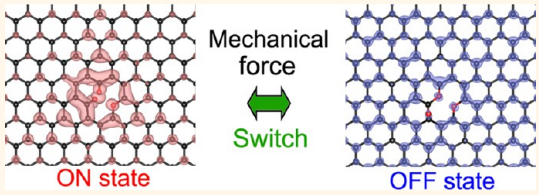

KEYWORDS: oxidized graphene · defect · electronic state · scanning probe microscopy · density functional theory

Graphene, which comprises a single atomic sheet of sp^2-hybridized carbon atoms, is a key building block for future generations of carbon-based electronic devices because of the tunability of its electronic and magnetic properties through nanofabrication and chemical modification.[1−8] Among techniques of tuning properties, the introduction of defects into graphene sheet is of particular importance, and extensive experimental efforts have focused on exploiting the defect-induced electronic states to functionalize graphene. The most widely discussed defect structures are linear defects of graphene edges and point defects in graphene plane.[8] Recent advances in structural and electronic characterization of the graphene edges,[2,7,9,10] combined with development of their nanofabrication processes based on (sono-)chemical,[11,12] lithographic,[13,14] and bottom-up synthetic[15−18] methods, have revealed that electronic properties of the graphene edges are crucially dependent on the atomic-scale-edge shapes. There are two typical graphene edge shapes that are referred to as zigzag and armchair shapes, in which qthe edges are terminated by carbon atoms belonging to one of sublattices and both of the paired sublattices in graphene bipartite lattice, respectively.[3−5,7,19−21] The zigzag-shaped edges support edge-localized nonbonding π state (edge state) located close to the Fermi energy, which originates from breaking of the local sublattice symmetry at the zigzag-edge-sites of the bipartite lattice,[7,19−21] while the armchair-shaped edges cause standing wave states with $\sqrt{3}a \times \sqrt{3}a$ periodicities (a = graphene lattice constant) near the edge regions, which come from the AB sublattice symmetry and can be explained by intervalley scattering of conduction electrons at the armchair edge boundary.[7,20−24] The edge state and standing wave in zigzag and armchair edges, respectively, are the source of the potential functionality in graphene. Namely, the edge state, which has a large local density of states at the Fermi energy with strong spin polarization, is the origin of electronic, chemical and magnetic activities in graphene edges,[25] while the standing wave is responsible for the stability of edges. Beyond the issue of the typical edge-shape dependent electronic properties, the effects of edge-terminated chemical

* Address correspondence to fujii.s.af@m.titech.ac.jp, tenoki@chem.titech.ac.jp.

Received for review September 22, 2013 and accepted November 9, 2013.

Published online November 09, 2013
10.1021/nn404937z

© 2013 American Chemical Society

functional groups[26−29] as well as reconstructed[30] and unreconstructed[31,32] chiral edge-shapes other than the typical ones on the electronic properties have been recently studied by means of scanning tunneling microcopy and transmission electron microscopy, in which atomic details at the edges, in fact, significantly alter the atomic-scale electronic properties.

Point defects possess edge-shape and edge-chemistry dependence on the electronic structures similar to that of extended linear edges. From experimental aspects, isolated point defects in graphene sheet have attracted much attention possibly due to their easier experimental accessibility, in which atomically sized defects are introduced by standard industrial irradiation technology. The introduction of defect structures, such as monatomic vacancies, adsorbed hydrogen defects,[33−35] and substitutional heteroatoms[36] into graphene breaks sublattice symmetry in the graphene bipartite lattice and is predicted to induce defect-localized nonbonding π states (defect edge state) in the vicinity of the Fermi level. Throughout this paper, the terms of "defect edge state" and "defect-localized edge state" are used to describe the defect-localized nonbonding π states around atomically sized defects in graphene plane, while the term "edge state" is used to refer to the localized nonbonding π states at the zigzag-shaped graphene edge.[20,21] Recent scanning probe microscopy (STM) studies have confirmed the existence of the defect edge states at monovacancy defects[37−40] and monosubstitutional nitrogen defect.[41] Together with the emergence of defect edge states, the monatomically sized point defects feature standing wave states around the defect sites,[37−40] which can originate from the short-range impurity potential localized at the defect sites that is a source of intervalley as well intravalley electron scattering.[42]

While the amount of research dealing with atomic-scale characterization of the linear defects with a variety of the edge-shapes and chemistry at the edges has increased,[26−32] a majority of the atomic-scale characterization on the point defects has been focused on several model systems such as pristine and/or reconstructed single vacancy defects,[37−40] a monohydrogen-adsorbed defect,[43] and a substitutional defect.[41] This is most probably due to the difficulty in introducing atomic-scale defects in a controlled manner. Introduction of chemical functional groups into the point defects as a form of chemically modified vacancy defects and chemical-functional-group-adsorbed defects (*i.e.*, on plane impurity defects) inevitably induces large out-of-plane deformation of graphene plane around the defects, which would lead to formation of several metastable structures. This inherent variability of defect structures in defective graphene has hampered detailed electronic characterization associated with the atomic-scale chemistry of the point defects.

Herein, we present the structural and electronic characterization of the point defects in defective graphene, which is prepared by chemical and thermal reduction of graphene oxide (GO).[44] High-resolution noncontact atomic force microscopy (NC-AFM) and conductive-AFM observations are utilized to investigate the low-energy π states (defect edge state) of atomic-scale defects in reduced GO and to correlate the results with realistic oxidized defect structures with the aid of density functional calculations. Finally, we demonstrate the dynamic behavior of the defect structures in which the defect-induced low-energy π state switches on and off upon rearrangement of the π-electron network, which is caused by a reversible change in the binding modes of the oxygen atoms in the oxidized defect.

RESULTS AND DISCUSSION

Chemical Reduction of Oxidized Graphene Sheets. Figure 1a shows an NC-AFM image of a single-layer GO sheet with a lateral size of ~500 nm × 500 nm. From extensive spectroscopic characterizations, it is known that COOH, OH, and C═O groups are present at the edge, while the basal plane is covered with mostly epoxide and hydroxyl groups, as shown in the structural model[45] in Figure 1b. To remove the oxygen-containing functional groups, the GO sheets were reduced by exposing them, on Au(111), to hydrazine vapor[46] followed by annealing at ~800 °C for 8 h under an ultrahigh vacuum. Previous X-ray photoelectron spectroscopy, Fourier-transform infrared spectroscopy, and thermogravimetry characterizations, density functional theory (DFT) simulations have demonstrated that GO is reduced through a combination of (i) ring-opening of the epoxide groups on the basal plane to form hydroxyl groups by chemical reduction and (ii) dehydroxylation by moderate heat treatment.[44] Desorption of OH radicals on the basal plane restores the π-electron network, while desorption at the edges yields σ radicals. The COOH groups at the edges are removed by thermal reduction at 100−150 °C.[44,47] However, the C═O moieties at the edges are much more stable and can only be reduced at temperatures as high as 1730 °C.[44,47] Therefore, carbonyl groups at the edges or defective edge sites (*i.e.*, atomic-scale vacancy edges in the basal plane) are rarely eliminated using the current reduction process. Figure 1c and d show current mapping images of GO sheets before and after chemical/thermal reduction, respectively. A significant increase in the vertical electronic conductivity and recovery of the π-electron network are apparent after reduction. Although reduction causes considerable loss of oxygen-containing functional groups, such as epoxide and hydroxyl groups, from the GO surface, oxidized defect structures remain in the basal plane. In the following section, we focus on atomic-scale characterization of the modulated

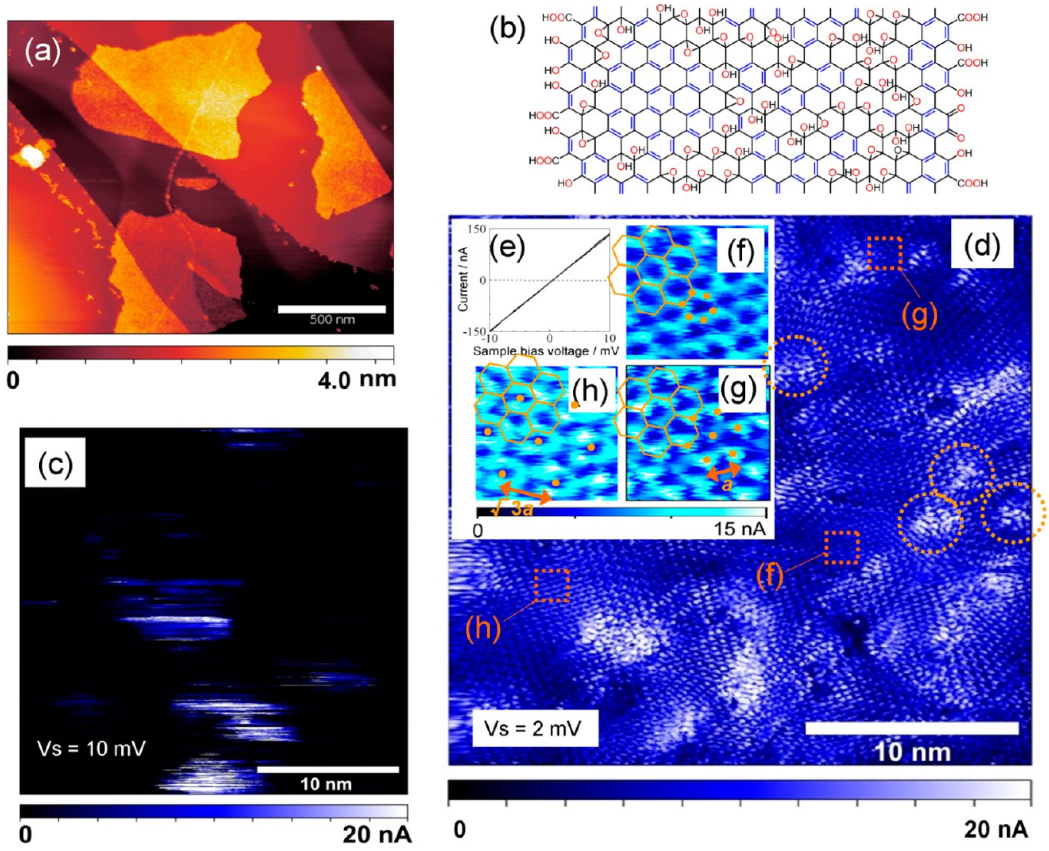

Figure 1. NC-AFM and conductive-AFM images of the GO sheets before and after reduction. (a) NC-AFM image of single-layer GO sheets on freshly cleaved highly oriented pyrolytic graphite (frequency shift = −10 Hz). (b) Structural model of GO, wherein the basal plane is modified by hydroxyl and epoxide functional groups. (c) Current-mapping image of GO on Au(111) before reduction recorded at a sample bias voltage (V_s) of 10 mV. Significant spatial variation in the vertical conductivity is apparent at the nanometer scale. The darker regions with almost no current signals are attributable to oxidized domains, while the patched conductive regions are nonoxidized graphene domains. (d) Current-mapping image of GO on Au(111) after chemical and thermal reduction (V_s = 2 mV). Dotted circles are guide for eye to indicate some of the atomically sized defects with higher LDOS. (e) Current *versus* bias voltage curves recorded on reduced graphene regions with clear honeycomb π-state patterns in the reduced GO sheet (−10 mV < V_s < +10 mV). (f−h) Current-mapping images of the π states of reduced GO taken at regions (f), (g), and (h) in image (d) as indicated by dotted square of 1.5 nm ×1.5 nm: (f) Honeycomb pattern that is typical for pristine graphene, (g) graphene sublattice pattern with a × a periodicity, and (h) superperiodic patterns with $\sqrt{3}a \times \sqrt{3}a$ periodicity (a = graphene lattice constant). Graphene honeycomb model (solid hexagons) and observed periodic patterns (orange dots) are schematically superimposed on each image. Image size is 1.5 nm × 1.5 nm.

electronic structure in the presence of the remaining oxidized defects.

High-Resolution Imaging of Atomic-Scale Defects in Reduced Graphene Oxide. In the small bias regime where the tunneling current is linearly dependent on the bias (Figure 1e), the tunneling current signal is proportional to the local density of states (LDOS) near the Fermi level (E_f), and thus basically reflects the π states of the reduced GO sheet. In the presence of metal substrate, E_f in reduced GO can be shifted from its original position because of the doping effect at the interface between graphene and substrate.[48−50] Previous STM studies have revealed that Dirac point is downshifted 0.35−0.4 eV upon interaction between exfoliated pristine graphene and polycrystalline gold,[48] while no appreciable doping exists on chemical-vapor-deposited graphene on Au(111).[49] A recent DFT study has demonstrated that graphene on Au(111) is either undoped or at most slightly p-type doped.[50] We believe that, in a similar manner to pristine graphene, interaction between reduced GO and Au(111) is weak enough and hole-doping effect is negligibly small.

In the reduced GO, bright protrusions, which are characterized by enhanced LDOS distributions, are distributed in defect regions as can be seen in Figure 1d. This demonstrates the presence of quasilocalized π states (defect edge state). The defect edge states exhibit a spatial distribution of 1−2 nm, which can be ascribed to atomically sized defect structures. Similar spatial distribution have been typically reported for defect-localized states of the monovacancy defects in graphite, in which the atomic sized defects show several nm-sized enhanced LDOS distribution with triangular shaped 3-fold symmetry.[37,38,40] Figure 1f−h shows high-resolution imaging of the electronic states (V_s = 2 mV) of the reduced GO sheets, which are taken in the region encircled with (f), (g), and (h) in Figure 1d. Figure 1g and h reveal that the LDOS distributions

differ noticeably from the honeycomb pattern (Figure 1f) that is typical for pristine graphene. The results of the LDOS distributions are summarized with (i) quasilocalized π states (defect edge states) with $a \times a$ periodicity (Figure 1g) and (ii) superperiodic pattern with $\sqrt{3}a \times \sqrt{3}a$ periodicities (a = graphene lattice constant) (Figure 1h). These experimental findings could be intuitively explained by the coexistence of zigzag and armchair geometries in the observed defects. The quasilocalized π states originate from the broken symmetry of the pseudospin (sublattice) in the graphene bipartite lattice.[7,22,35] Nearest-neighbor tight binding models for the electronic states of vacancies in graphene planes have demonstrated that if the distribution of π vacancies between the two sublattices is uneven, zero-energy modes (*i.e.*, the quasilocalized defect edge states) will appear.[51] Topological lattice defects such as adsorbed defects on the graphene lattice also break the local sublattice symmetry by removing a π electron from the graphene-π-electron network. DFT studies have demonstrated that single impurity defects such as "monovacancy", "adsorbed hydrogen", and "adsorbed hydroxyl" defects, which have broken sublattice symmetry, induce quasilocalized zero-energy states at nearest neighbor carbon sites around the defect.[33−35,52] The quasilocalized zero-energy-states decay into bulk with a finite amplitude at sites in one of the graphene sublattices, which manifests $a \times a$ periodic patterns. In contrast, such zero-energy states vanish for an "adsorbed epoxide" defect,[52] which removes two π electrons from a pair of neighboring A and B carbon-sublattice sites in graphene plane (it should also be noted that the zero-mode state necessarily appears in the sublattice-imbalanced system, while it does not always vanish in a sublattice-balanced system). In analogy with the single-impurity defects, oxidized defect structures in the reduced GO can break the local sublattice symmetry and cause unique edge-localized π states.

The superperiodic patterns with $\sqrt{3}a \times \sqrt{3}a$ periodicities (Figure 1h) arise from a standing wave formation due to intervalley scattering of conduction electrons at defect sites (*e.g.*, see refs 23, 24) or defect-induced electronic gap formation due to electron−lattice interactions (*i.e.*, charge-density wave formation in the π states near E_f) (*e.g.*, see refs 22, 53). Similar modulated LDOS with the superperiodic patterns has been commonly identified around atomically sized defects in graphene materials.[37−40,49]

A more detailed characterization of the electronic structures in the two different kinds of defect-induced states is presented with DFT simulations in the later section. In the following section, we focus on dynamic behavior of the edge-localized π state.

Reversible Switching of the Defect-Localized State in Reduced Graphene Oxide. Interestingly, we observed drastic on−off switching of the defect-localized π states in reduced GO during repeated imaging, indicating that the geometry of the π-electron network around the defect can be reconstructed. About ~10% of the atomic-scale defects undergo a dramatic switch of the enhanced LDOS at E_f. Higher resolution imaging shows that the "ON" state in Figure 2a and b exhibits enhanced LDOS distribution with a triangular pattern at the defect, which decays into the bulk with an exponential decay length of ~0.3 nm and $a \times a$ periodicity (Figure 2c), while the "OFF" state in Figure 2d and e is characterized by a complete disappearance of the enhanced LDOS (*i.e.*, bright spots) and evolution of the extended superperiodic patterns with $\sqrt{3}a \times \sqrt{3}a$ periodicity near the defect region (Figure 2c).

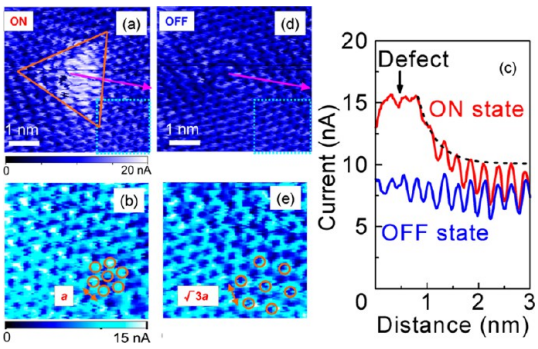

Figure 2. Reversible on−off switching of a defect-localized state. (a) High-resolution images of the π state of the ON state in the defects of reduced GO (V_s = 2 mV). Triangular pattern is a guide for the eye and is superimposed on the image. (b) Magnified image of the vicinity of the defect indicated by the dotted square in (a) in which $a \times a$ periodicity is shown schematically. (c) Averaged cross-sectional profiles from the defect site to the bulk region along the typical graphene crystallographic direction, as indicated by the arrows in the ON and OFF state images ((a) and (d), respectively). The dotted line for the ON state indicates exponential curve fitting with a decay length of 0.3 nm. (d) High-resolution images of the π state of the OFF state (V_s = 2 mV). (e) Magnified image of the area around the dotted square region in (d); $\sqrt{3}a \times \sqrt{3}a$ periodicity is superimposed on the image.

To investigate the dynamic on−off switching behavior, a series of LDOS images around the defect were recorded at 17 min intervals, during which reversible switching between the ON and OFF states occurs several times (Figure 3). Among the 28 images recorded, (2), (12), (24), and (27) (Figure 3) show abrupt switching events induced by the raster scanning of the AFM tip. This scan-induced switching occurs in both the ON-to-OFF and OFF-to-ON directions. Halfway through the upward raster imaging in image (27), the OFF state suddenly switches to the ON state (Figure 4a) when the AFM tip scans just across the defect site, as shown in the scan profiles (Figure 4b). The AFM-tip-induced local mechanical force on the defect induces structural deformation around the defect, which could eventually modify the bond configurations.

Concurrent with the scan-induced direct switching, thermally activated stochastic switching occurs, which

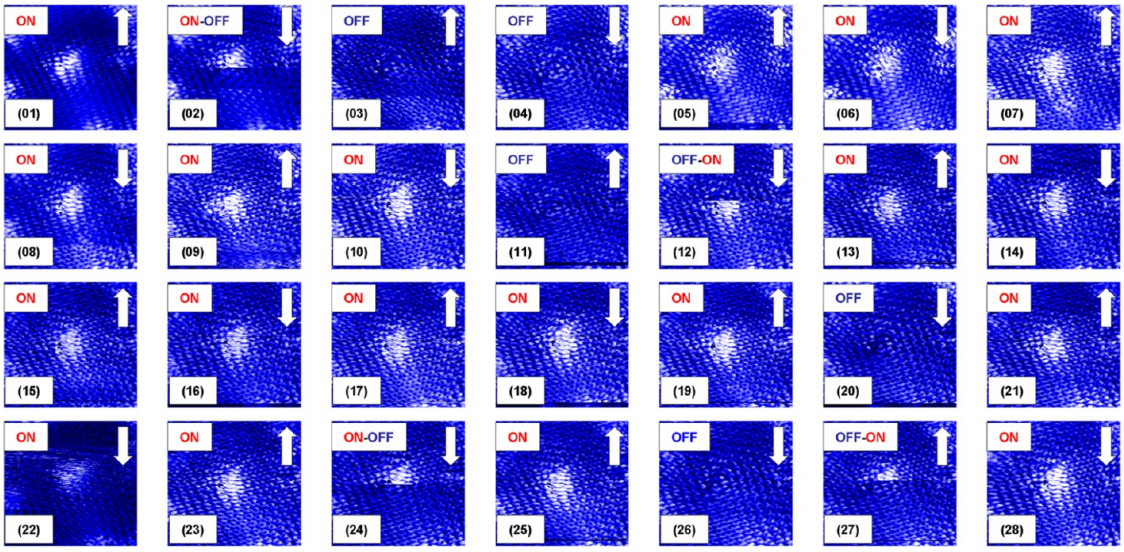

Figure 3. Switching behavior of the defect-localized state. A series of high-resolution images of the π state at the oxidized defect, which is subject to on−off switching of the defect-localized state ($V_s = 2$ mV). Image size is 7.5 nm × 7.5 nm. Each image is recorded by raster scanning the AFM tip at 17 min intervals. The fast scan direction is from left to right (horizontal), and the slow scan direction (vertical) is represented by a white arrow in each image. In images (2), (12), (24), and (27), scan-induced switching behaviors are observed when the AFM tip is scanned across the defect site. Consequently, the LDOS patterns suddenly change halfway through the imaging of the defect site. The ON state switched to the OFF state in images (2) and (24) (*i.e.*, the bright protrusion disappeared halfway through the imaging of the defect site), and the OFF state switched to the ON state in images (12) and (27) (*i.e.*, the bright protrusion appeared halfway through the imaging of the defect site).

causes ~80% of the observed states without the scan-induced direct switching event to be in the ON state (Figure 4c). It should be noted that a reversible structural change in an AFM-tip apex (*i.e.*, change in the electronic state of the tip) may explain the switching of the appearance of the LDOS at the defect site. Generally, tip structural changes switch the LDOS patterns of not only the defect site but also the whole sample surface area, which does not occur in this case. Thus the switching of the LDOS patterns that are observed only at the defect sites is attributable to not just a structural change of the tip apex but a structural change of the defects.

As a result of the chemical/thermal reduction process studied here, oxidized structures in the basal plane most likely comprise atomic-scale vacancy edges modified with σ dangling bonds and oxygen atoms, as discussed in the previous section. To identify the optimal defect structure for reversibly switchable bond configurations, which lead to the evolution and disappearance of the edge-localized state, DFT calculations within the local density approximation (LDA) were performed using graphene supercell models with mono- and dicarbon vacancies modified by oxygen atoms. The initial atomic configurations were generated with the oxygen atoms on the top and/or bottom of the vacancy-edge sites in the graphene supercell.[54] The atomic positions were then relaxed to the closest local minimum of the LDA total energy. Among the metastable configurations found in the structural relaxation (Figure 5), the interconvertible forms of (2i−2ii), (3i−3ii), (6i−6ii), and (7i−7ii) exhibit on−off switching in the edge-localized state with the reversible configurational changes (see Supporting Information SI-1). The calculated total energy differences between the two configurations in (2), (3), (6), and (7) are approximately +4 eV ($E_{2i} - E_{2ii}$),[54] +2.5 eV ($E_{3i} - E_{3ii}$), −0.1 eV ($E_{6i} - E_{6ii}$), and −0.3 eV ($E_{7i} - E_{7ii}$), respectively, which indicates that the reversible configurational switch in (2) and (3) is unlikely because of the larger energy differences between the two configurations. During the configurational switch from (6i) to (6ii) (Figure 5), two carbonyl bonds at the vacancy edges convert into two ether moieties in a concerted manner (Figure 6a and b). Consequently, the hybridization of the two oxygen atoms changes from sp^2 to sp^3, which leads to significant rearrangement of the π-electron network around the vacancy-edge sites. In contrast to the sp^3-hybridized oxygen atom in the ether groups, the sp^2-hybridized oxygen atom in the carbonyl group has a free p_z orbital, which can participate into the graphene π-electron network.

On the basis of DFT-LDA using linear and quadratic synchronous transit methods, as implemented in CASTEP code, the energy barrier of switching from (6i) to (6ii) is estimated to be 0.8 eV; however, no reaction path was evident for the transition between (7i) and (7ii) (see Supporting Information SI-2). During switching between (7i) and (7ii), the steric interactions of the four carbonyl groups cause large energetic destabilization and impede the transition between (7i) and (7ii) (see Supporting Information SI-2).

While other scenarios that involve a wide variety of chemical functional groups other than oxygen at the

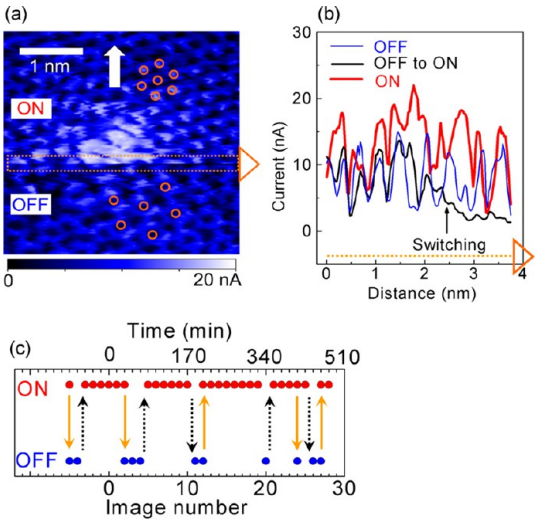

Figure 4. Scan-induced on−off switching of the localized state and time evolution of the switching behavior. (a) Magnified high-resolution images of the π state in image (27) (Figure 3); the slow scan direction is indicated by an arrow. The OFF state suddenly switched to the ON state when the AFM tip scanned across the defect site. (b) Averaged cross-sectional profiles along the dotted arrow in (a) before and after switching. The switching event is characterized by an abrupt decrease in current and is indicated by an arrow in the current profile. The direction of the profiles is denoted by the dotted arrow. (c) Switching behavior as a function of time (image number in Figure 3). Images (−5) to (0) are not shown in Figure 3. The filled arrows denote scan-induced switching events (*i.e.*, when the localized state suddenly turns on or off as the AFM tip scans across the defect site), while the dotted arrows indicate stochastic switching events. Beside the scan-induced switching events, stochastic switching process (*e.g.*, see image numbers from (4) to (5), from (−4) to (−3), from (10) to (11), from (19) to (20), from (20) to (21) in c) are also observed, in which the state switches on and off without external mechanical perturbation induced by AFM-tip-scanning. Among the total of 34, 5 images show the scan-induced switching. Among the remaining 29 images without the switching events, 23 images (*i.e.*, ~80%) exhibit the ON state.

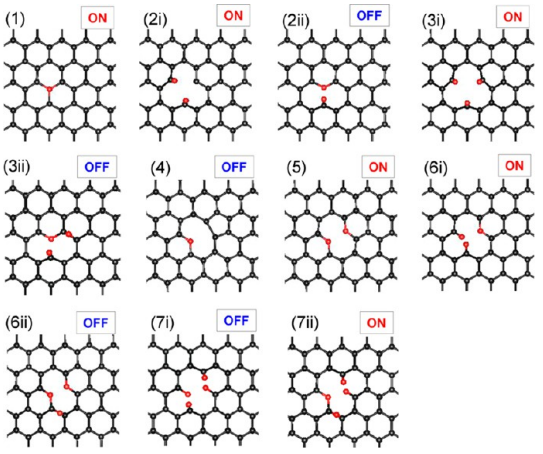

Figure 5. DFT-relaxed structures of oxidized vacancy edges in graphene supercells. (1−3) Oxidized monovacancy edges with 1−3 oxygen atoms, and (4−7) oxidized divacancy edges with 1−4 oxygen atoms. Oxygen atoms are denoted with red circles. For models 2, 3, 6, and 7, there are two structures with the same stoichiometry, which are labeled (i) and (ii). On the basis of DFT calculations, the presence and absence of the edge-localized state are labeled by "ON" and "OFF" on the right corner in each model, respectively.

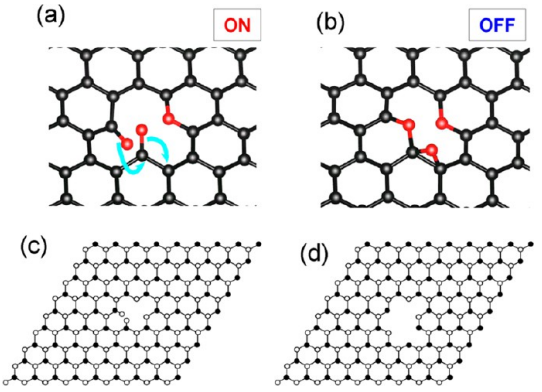

Figure 6. (a) and (b) Top perspective of the two configurations of (6), *i.e.*, (6i) and (6ii), with and without an edge-localized π state, respectively. Two carbonyl bonds at the vacancy edges of (6i) can convert into two ether moieties (6ii) in a concerted manner. Electron movement is indicated by single-headed arrows. Oxygen atoms are represented by red circles. (c) and (d) Simplified π-site models of (6i) and (6ii). Black and white balls represent the π-sites belonging to A(B) and B(A) sublattices, respectively. The sp^3-hybridized oxygen site in the ether group and the sp^3-hybridized two carbon sites without free p_z orbitals cannot act as effective π-site-vacancies. The sp^2-hybridized oxygen site in the carbonyl group with a p_z orbital can act as an effective π-site. The white balls singly bonded in the defect periphery in (c) are oxygen atoms belonging to a sublattice same as that of carbon atoms marked with white balls.

defect edges undergoing reversible structural changes are possible, only switching of the bonding patterns of oxygen between carbonyl (sp^2-hybridized) and ether (sp^3-hybridized) forms rearranges the π-electron network without considerable energetic destabilization due to breakage of chemical bonds (see Supporting Information SI-3). Taking into account the on−off switching of the edge localized states along with the reversible structural changes, the scenario can be limited to switching behaviors associated with concerted reactions where the bonding configurations of two oxygen atoms at the defect edges convert from sp^2- to sp^3-hybridization within the mono- and divacancy edge models studied here (see Supporting Information SI-3).

The oxidation-induced rearrangement of the π-electron network (*i.e.*, the local sublattice symmetry) could be intuitively modeled by considering that (i) the π electrons in the ether group do not participate in the graphene π-electron network,[55] (ii) the carbonyl groups add an additional π-site to the graphene π-system around the defect edges,[29,55] and (iii) the epoxide group removes the neighboring π-sites of the graphene lattice.[52] On the basis of these simple guidelines, the π-electron networks in the defect structures of (6i) (ON state) and (6ii) (OFF state) can be represented, as shown in Figure 6c and d, respectively.

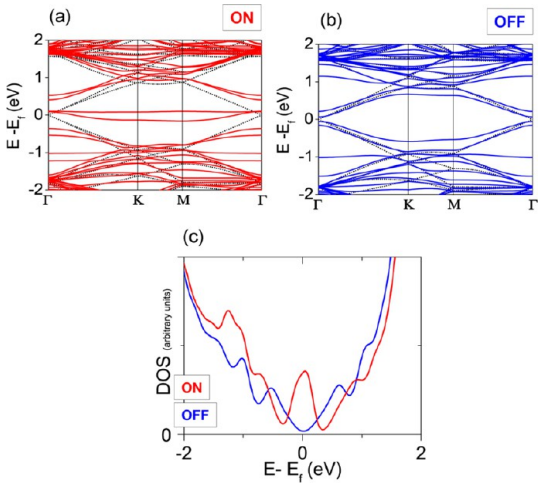

Figure 7. DFT-calculated band structures and DOSs of the ON and OFF states of configurations (6i) and (6ii), respectively. (a) and (b) Band structures of the (a) ON and (b) OFF states along the high symmetry points (Γ-K-M-Γ). The dotted lines correspond to the band structure of pristine graphene obtained from a similar calculation method. (c) DOSs of the ON and OFF states.

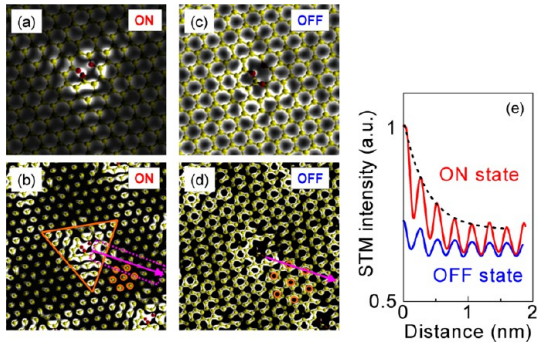

Figure 8. (a−d) Simulated current-mapping images of the (a, b) ON and (c, d) OFF states superimposed on their structural models (V_s = +0.3 V). The ON and OFF states correspond to (6i) and (6ii), respectively. In (b) and (d), the image contrast is enhanced. The triangular pattern, $a \times a$ periodicity of the ON state, and $\sqrt{3}a \times \sqrt{3}a$ periodicity of the OFF state are schematically shown in the images. (e) Averaged cross-sectional profiles of the simulated images along the same directions as the experimental profiles (Figure 2c). The directions are denoted by arrows in the ON- and OFF-state images. The STM intensities are normalized to the maximum value of the ON state. The dotted line for the ON state indicates exponential curve fitting. The exponential decay length is estimated to be 0.35 nm, which is in good agreement with the experimental value of ~0.3 nm (see main text).

The benzenoid graph theory[35] predicts that the zero-energy state (edge state) appears when the sublattice sites in a π-electron network are imbalanced (*i.e.*, $\Delta N \neq 0$ where $\Delta N = |N_A - N_B|$, where N_A and N_B are the numbers of π-sites in sublattices A and B, respectively). In a crude approximation, ΔN can be estimated by counting the sublattice sites per unit cell in Figure 6c and d. A simple analysis of the sublattice imbalance demonstrates that ΔN is nonzero for the ON state [(6i)] and zero for the OFF state [(6ii)], which indicates that the on−off switching behavior can be understood in terms of breaking the sublattice symmetry (*i.e.*, a sublattice imbalance). A similar explanation is valid for the on−off switching in (2), (3), and (7). For a more in-depth discussion, the significant out-of-plane deformations of the carbonyl groups in the oxidized edges of (2), (3), (6i), and (7) and the relevant contribution of the oxygen π-electrons into the graphene π-system should be carefully considered.

The calculated band structures and DOSs for the two configurations (Figure 6) are shown in Figure 7: The ON state exhibits a sharp DOS peak at E_f that originates from nearly flat bands of the defect-localized edge state near E_f (Figure7a and c), whereas the OFF state does not have such state (Figure 7b and c). The ON state is energetically more stable than the OFF state (see Figure S2, Supporting Information), which is consistent with the preferential emergence of the ON state during the stochastic switching process (Figure 4c). The higher stability of the ON state could be derived from the energetic destabilization of the OFF state that occurs because of the structural distortion induced by the on-plane ether group (*i.e.*, the epoxide). In the LDA-relaxed structures (Figure 6a and b), the large strain can be recognized as an exceptionally elongated carbon−carbon bond in the epoxy ring (Figure 6b), in which the bond length is deviated 7% (*i.e.*, 0.153 nm) from the equilibrium length (*i.e.*, 0.142 nm), whereas the deviations are less than 4% for remaining carbon−carbon bonds at the periphery of defects (Figure 6a and b).

DFT-simulated current-mapping images within the Tersoff−Hamann approximation[56,57] indicate that (i) the LDOS at E_f (Figure 7c) for the ON state is strongly localized at the vacancy edge sites, which decay into the bulk with a finite amplitude at one of the graphene-sublattice sites (Figure 8a and b) and (ii) the edge-localized π state is quenched for the OFF state, in which extended π state propagates around the defect region to form a superperiodic pattern of $\sqrt{3}a \times \sqrt{3}a$ periodicity (Figure 8c and d). A closer look at the simulated images reveals that the decaying π state distribution with $a \times a$ periodicity for the ON state and the extended π state with $\sqrt{3}a \times \sqrt{3}a$ periodicity for the OFF state correlate well with the experimentally observed patterns (Figure 2). The triangular patterns with asymmetric localized state distributions in the ON state (*i.e.*, at one of the three vertices of the triangular pattern that has a localized state with a much lower amplitude) are in qualitative agreement with the experimental data, while the complete disappearance of the edge-localized state in the OFF state is evident from both theoretical and experimental results.

CONCLUSION

In summary, we successfully reduced GO on Au(111) and characterized it by scanning probe microscopy.

The current-mapping images reveal that the LDOS of the reduced GO is considerably different from that of pristine graphene. The LDOS distributions are characterized by (i) extended superperiodic patterns with $\sqrt{3}a \times \sqrt{3}a$ periodicity as a result of intervalley scattering of conduction electrons and (ii) a defect-localized edge state that decays into the bulk with $a \times a$ periodicity originating from breaking the symmetry of the pseudospin in the graphene bipartite lattice. Atomic-scale oxidized vacancy edge defects feature on−off switching of the defect-localized π state, which is explained by a tip-induced reversible change in the oxidized structures, as determined by DFT calculations. The π-electron network around the defect depends on the binding mode of the C−O bonds (*i.e.*, either sp^2-hybridized carbonyl or sp^3-hybridized ether bonds) in the oxidized vacancy defect. Consequently, the evolution and disappearance of the defect-localized π state (*i.e.*, local sublattice symmetry) can be modulated through the C−O binding mode, which can be controlled by tip-induced external mechanical perturbations, as demonstrated in the AFM manipulation experiment. This study reveals that precise control of the oxidized structures is crucial for the emergence of the unique defect-localized π state in reduced GO samples, which could be an important aspect of future graphene-based electronic/magnetic devices.

METHODS

Sample Preparation. GO samples were prepared from natural graphite (Kojundo Chemical Laboratory) using the conventional Hummers method[58] and drop-cast onto freshly cleaved highly ordered pyrolytic graphite or Au(111) substrates. The Au(111) substrates were prepared *via* the thermal evaporation of Au onto mica. The GO sheets on Au(111) underwent hydrazine reduction through exposure to hydrazine monohydrate (Kanto Chemical Co., Inc.) vapor. The resultant hydrazine-exposed GO sheets were then thermally reduced by heating on Au(111) at 800 °C for 8 h under UHV.

AFM Characterization. All AFM measurements were performed under UHV ($\sim 5 \times 10^{-8}$ Pa) at room temperature using a commercially available AFM system (VT beam-deflection AFM, Omicron). NC-AFM was performed using a phase-locked loop unit (Easy PLL-plus, Nanosurf) for frequency modulation feedback.[59] NC-AFM images were acquired using a silicon cantilever (NSC11, Micromash) or titanium−platinum-coated silicon cantilever (NSC11/Ti−Pt). The cantilevers were oscillated at a constant peak-to-peak amplitude of ~20 nm at their resonant frequencies. The resonant frequencies and force constants of the cantilevers were 350−450 kHz and 40−50 N/m, respectively. Current mapping was performed using a platinum-coated silicon cantilever (CONTPt, Nanosensors) with a spring constant of 0.2 N/m. During imaging, a force of ~10 nN and a bias voltage of ±0.002−0.150 V were maintained. Within this bias range, no significant change in the contrast of the current-mapping image was observed. Typically, simultaneously obtained topographic images exhibited no atomic contrast; therefore, only tunneling-current images are presented here.

DFT Calculations. DFT calculations were performed within the LDA using the Perdew−Zunger exchange correlation[60] scheme, as implemented in the PWSCF code of the Quantum-ESPRESSO package.[61] Rectangular graphene supercells containing 72 carbon atoms (1.476 nm × 1.278 nm) and hexagonal supercells containing 162 carbon atoms ($9a \times 9a$; $a = 0.246$ nm) were used for modeling of the oxidized structures in Figure 5 and Figures 7 and 8, respectively. The defect structures were made by (i) removing one or two carbon atoms from pristine graphene and (ii) placing oxygen atoms on the vacancy edges.[54] For the ultrasoft pseudopotentials adopted here, the cutoff energy for the expansion of the wave functions was set at 25 Ry for calculating the optimized geometries. All atoms were fully relaxed until the forces were less than 10^{-3} Ry/a.u. For simulations of the current-mapping images, the wave function cutoff energy was set at 60 Ry. Brillouin-zone integration was performed using a uniform $8 \times 8 \times 1$ Monkhorst-type k-point grid.[62]

Conflict of Interest: The authors declare no competing financial interest.

Acknowledgment. This work was supported by Grants-in-Aid for Scientific Research (No. 20001006, No. 23750150, and No. 25790002) from the Ministry of Education, Culture, Sports, Science and Technology of Japan.

Supporting Information Available: (SI-1) LDA-calculated band structures for the models (2i), (2ii), (3i), (3ii), (7i), and (7ii). (SI-2) Estimation of the energy barrier between the ON and OFF states. (SI-3) Proposed oxidized defect models. Figures S1−S9. This material is available free of charge *via* the Internet at http://pubs.acs.org.

REFERENCES AND NOTES

1. Bekyarova, E.; Sarkar, S.; Wang, F.; Itkis, M. E.; Kalinina, I.; Tian, X.; Haddon, R. C. Effect of Covalent Chemistry on the Electronic Structure and Properties of Carbon Nanotubes and Graphene. *Acc. Chem. Res.* **2013**, *46*, 65–76.
2. Jia, X.; Campos-Delgado, J.; Terrones, M.; Meunier, V.; Dresselhaus, M. S. Graphene Edges: a Review of Their Fabrication and Characterization. *Nanoscale* **2011**, *3*, 86–95.
3. Loh, K. P.; Bao, Q.; Ang, P. K.; Yang, J. The Chemistry of Graphene. *J. Mater. Chem.* **2010**, *20*, 2277–2289.
4. Rao, C. N. R.; Sood, A. K.; Subrahmanyam, K. S.; Govindaraj, A. Graphene: The New Two-Dimensional Nanomaterial. *Angew. Chem., Int. Ed.* **2009**, *48*, 7752–7777.
5. Müllen, K.; Rabe, J. P. Nanographenes as Active Components of Single-Molecule Electronics and How a Scanning Tunneling Microscope Puts Them to Work. *Acc. Chem. Res.* **2008**, *41*, 511–520.
6. Ruoff, R. Calling All Chemists. *Nat. Nanotechnol.* **2008**, *3*, 10–11.
7. Enoki, T. Role of Edges in the Electronic and Magnetic Structures of Nanographene. *Phys. Scr., T* **2012**, *146*, 014008−1–14.
8. Banhart, F.; Kotakoski, J.; Krasheninnikov, A. V. Structural Defects in Graphene. *ACS Nano* **2011**, *5*, 26–41.
9. Zhang, X.; Xin, J.; Ding, F. The Edges of Graphene. *Nanoscale* **2013**, *5*, 2556–2569.
10. Kobayashi, Y.; Fukui, K.; Enoki, T.; Kusakabe, K.; Kaburagi, Y. Observation of Zigzag and Armchair Edges of Graphite Using Scanning Tunneling Microscopy and Spectroscopy. *Phys. Rev. B: Condens. Matter Mater. Phys.* **2005**, *71*, 193406.
11. Kosynkin, D. V.; Higginbotham, A. L.; Sinitskii, A.; Lomeda, J. R.; Dimiev, A.; Price, B. K.; Tour, J. M. Longitudinal Unzipping of Carbon Nanotubes to Form Graphene Nanoribbons. *Nature* **2009**, *458*, 872–876.
12. Tao, C.; Jiao, L.; Yazyev, O. V.; Chen, Y.-C.; Feng, J.; Zhang, X.; Capaz, R. B.; Tour, J. M.; Zettl, A.; Louie, S. G.; *et al.* Spatially Resolving Edge States of Chiral Graphene Nanoribbons. *Nat. Phys.* **2011**, *7*, 616–620.
13. Jiao, L.; Zhang, L.; Wang, X.; Diankov, G.; Dai, H. Narrow Graphene Nanoribbons from Carbon Nanotubes. *Nature* **2009**, *458*, 877–880.

14. Girit, Ç. Ö.; Meyer, J. C.; Erni, R.; Rossell, M. D.; Kisielowski, C.; Yang, L.; Park, C.-H.; Crommie, M. F.; Cohen, M. L.; Louie, S. G.; *et al.* Graphene at the Edge: Stability and Dynamics. *Science* **2009**, *323*, 1705–1708.
15. Chen, L.; Hernandez, Y.; Feng, X.; Müllen, K. From Nanographene and Graphene Nanoribbons to Graphene Sheets: Chemical Synthesis. *Angew. Chem., Int. Ed.* **2012**, *51*, 7640–7654.
16. Huang, H.; Wei, D.; Sun, J.; Wong, S. L.; Feng, Y. P.; Neto, A. H. C.; Wee, A. T. S. Spatially Resolved Electronic Structures of Atomically Precise Armchair Graphene Nanoribbons. *Sci. Rep.* **2013**, *2*, 983.
17. Konishi, A.; Hirao, Y.; Matsumoto, K.; Kurata, H.; Kishi, R.; Shigeta, Y.; Nakano, M.; Tokunaga, K.; Kamada, K.; Kubo, T. Synthesis and Characterization of Quarteranthene: Elucidating the Characteristics of the Edge State of Graphene Nanoribbons at the Molecular Level. *J. Am. Chem. Soc.* **2013**, *135*, 1430–1437.
18. Morita, Y.; Suzuki, S.; Sato, K.; Takui, T. Synthetic Organic Spin Chemistry for Structurally Well-Defined Open-Shell Graphene Fragments. *Nat. Chem.* **2011**, *3*, 197–204.
19. Sasaki, K.; Saito, R. Pseudospin and Deformation-Induced Gauge Field in Graphene. *Prog. Theor. Phys. Suppl.* **2008**, *176*, 253–278.
20. Fujita, M.; Wakabayashi, K.; Nakada, K.; Kusakabe, K. Peculiar Localized State at Zigzag Graphite Edge. *J. Phys. Soc. Jpn.* **1996**, *65*, 1920–1923.
21. Nakada, K.; Fujita, M.; Dresselhaus, G.; Dresselhaus, M. S. Edge State in Graphene Rribbons: Nanometer Size Effect and Edge Shape Dependence. *Phys. Rev. B: Condens. Matter Mater. Phys.* **1996**, *54*, 17954–17961.
22. Fujii, S.; Enoki, T. Nanographene and Graphene Edges: Electronic Structure and Nanofabrication. *Acc. Chem. Res.* **2013**, *46*, 2202–2210.
23. Yang, H.; Mayne, A. J.; Boucherit, M.; Comtet, G.; Dujardin, G.; Kuk, Y. Quantum Interference Channeling at Graphene Edges. *Nano Lett.* **2010**, *10*, 943–947.
24. Park, C.; Yang, H.; Mayne, A. J.; Dujardin, G.; Seo, S.; Kuk, Y.; Ihm, J.; Kim, G. Formation of Unconventional Standing Waves at Graphene Edges by Valley Mixing and Pseudospin Rotation. *Proc. Natl. Acad. Sci. U. S. A.* **2011**, *108*, 18622–18625.
25. Enoki, T.; Takai, K. The Edge State of Nanographene and the Magnetism of the Edge-State Spins. *Solid State Commun.* **2009**, *149*, 1144–1150.
26. Talirz, L.; Söde, H.; Cai, J.; Ruffieux, P.; Blankenburg, S.; Jafaar, R.; Berger, R.; Feng, X.; Müllen, K.; Passerone, D.; *et al.* Termini of Bottom-Up Fabricated Graphene Nanoribbons. *J. Am. Chem. Soc.* **2013**, *135*, 2060–2063.
27. Kobayashi, Y.; Fukui, K.; Enoki, T.; Kusakabe, K. Edge State on Hydrogen-Terminated Graphite Edges Investigated by Scanning Tunneling Microscopy. *Phys. Rev. B: Condens. Matter Mater. Phys.* **2006**, *73*, 125415.
28. Ziatdinov, M.; Fujii, S.; Kusakabe, K.; Kiguchi, M.; Mori, T.; Enoki, T. Visualization of Electronic States on Atomically Smooth Graphitic Edges with Different Types of Hydrogen Termination. *Phys. Rev. B: Condens. Matter Mater. Phys.* **2013**, *87*, 115427.
29. Ohtsuka, M.; Fujii, S.; Kiguchi, M.; Enoki, T. Electronic State of Oxidized Nanographene Edge with Atomically Sharp Zigzag Boundaries. *ACS Nano* **2013**, *7*, 6868–6874.
30. Pan, M.; Girao, E. C.; Jia, X.; Bhaviripudi, S.; Li, Q.; Kong, J.; Meunier, V.; Dresselhaus, M. S. Topographic and Spectroscopic Characterization of Electronic Edge States in CVD Grown Graphene Nanoribbons. *Nano Lett.* **2012**, *12*, 1928–1933.
31. Zhang, X.; Yazyev, O. V.; Feng, J.; Xie, L.; Tao, C.; Chen, Y.-C.; Jiao, L.; Pedramrazi, Z.; Zettl, A.; Louie, S. G.; *et al.* Experimentally Engineering the Edge Termination of Graphene Nanoribbons. *ACS Nano* **2013**, *7*, 198–202.
32. Suenaga, K.; Koshino, M. Atom-by-Atom Spectroscopy at Graphene Edge. *Nature* **2010**, *468*, 1088–1090.
33. Yazyev, O. V.; Helm, L. Defect-Induced Magnetism in Graphene. *Phys. Rev. B: Condens. Matter Mater. Phys.* **2007**, *75*, 125408.
34. Boukhvalov, D. W.; Katsnelson, M. I.; Lichtenstein, A. I. Hydrogen on Graphene: Electronic Structure, Total Energy, Structural Distortions and Magnetism from First-Principles Calculations. *Phys. Rev. B: Condens. Matter Mater. Phys.* **2008**, *77*, 035427.
35. Yazyev, O. V. Emergence of Magnetism in Graphene Materials and Nanostructures. *Rep. Prog. Phys.* **2010**, *73*, 056501.
36. Hou, Z.; Wang, X.; Ikeda, T.; Terakura, K.; Oshima, M.; Kakimoto, M. Electronic Structure of N-Doped Graphene with Native Point Defects. *Phys. Rev. B: Condens. Matter Mater. Phys.* **2013**, *87*, 165401.
37. Kelly, K. F.; Sarkar, D.; Hale, G. D.; Oldenburg, S. J.; Halas, N. J. Threefold Electron Scattering on Graphite Observed with C60-Adsorbed STM Tips. *Science* **1996**, *273*, 1371–1373.
38. Ruffieux, P.; Melle-Franco, M.; Gröning, O.; Bielmann, M.; Zerbetto, F.; Gröning, P. Charge-Density Oscillation on Graphite Induced by the Interference of Electron Waves. *Phys. Rev. B: Condens. Matter Mater. Phys.* **2005**, *71*, 153403.
39. Rutter, G. M.; Crain, J. N.; Guisinger, N. P.; Li, T.; First, P. N.; Stroscio, J. A. Scattering and Interference in Epitaxial Graphene. *Science* **2007**, *317*, 219–222.
40. Ugeda, M. M.; Brihuega, I.; Guinea, F.; Gómez-Rodríguez, J. M. Missing Atom as a Source of Carbon Magnetism. *Phys. Rev. Lett.* **2010**, *104*, 096804.
41. Zhao, L.; He, R.; Rim, K. T.; Schiros, T.; Kim, K. S.; Zhou, H.; Gutiérrez, C.; Chockalingam, S. P.; Arguello, C. J.; Pálová, L.; *et al.* Visualizing Individual Nitrogen Dopants in Monolayer Graphene. *Science* **2011**, *333*, 999–1003.
42. Matis, B. R.; Houston, B. H.; Baldwin, J. W. Low-Energy Resonant Scattering from Hydrogen Impurities in Graphene. *Phys. Rev. B: Condens. Matter Mater. Phys.* **2013**, *88*, 085441.
43. Balog, R.; Jørgensen, B.; Wells, J.; Lægsgaard, E.; Hofmann, P.; Besenbacher, F.; Hornekær, L. Atomic Hydrogen Adsorbate Structures on Graphene. *J. Am. Chem. Soc.* **2009**, *131*, 8744–8745.
44. Pei, S.; Cheng, H.-M. The Reduction of Graphene Oxide. *Carbon* **2012**, *50*, 3210–3228.
45. Lerf, A.; He, H.; Forster, M.; Klinowski, J. Structure of Graphite Oxide Revisited. *J. Phys. Chem. B* **1998**, *102*, 4477–4482.
46. Watcharotone, S.; Dikin, D. A.; Stankovich, S.; Piner, R.; Jung, I.; Dommett, G. H. B.; Evmenenko, G.; Wu, S. E.; Chen, S. F.; Liu, C-Pu.; *et al.* Graphene-Silica Composite Thin Films as Transparent Conductors. *Nano Lett.* **2007**, *7*, 1888–1892.
47. Gao, X.; Jang, J.; Nagase, S. Hydrazine and Thermal Reduction of Graphene Oxide: Reaction Mechanisms, Product Structures, and Reaction Design. *J. Phys. Chem. C* **2010**, *114*, 832–842.
48. Klusek, Z.; Dabrowski, P.; Kowalczyk, P.; Kozlowski, W.; Olejniczak, W.; Blake, P.; Szybowicz, M.; Runka, T. Graphene on Gold: Electron Density of States Studies by Scanning Tunneling Spectroscopy. *Appl. Phys. Lett.* **2009**, *95*, 113114.
49. Martínez-Galera, A. J.; Brihuega, I.; Gómez-Rodríguez, J. M. Ethylene Irradiation: A New Route to Grow Graphene on Low Reactivity Metals. *Nano Lett.* **2011**, *11*, 3576–3580.
50. Sławińska, J.; Dabrowski, P.; Zasada, I. Doping of Graphene by a Au(111) Substrate: Calculation Strategy within the Local Density Approximation and a Semiempirical Van Der Waals Approach. *Phys. Rev. B: Condens. Matter Mater. Phys.* **2010**, *83*, 245429.
51. Pereira, V. M.; dos Santos, J. M. B. L.; Neto, A. H. C. Modeling Disorder in Graphene. *Phys. Rev. B: Condens. Matter Mater. Phys.* **2008**, *77*, 115109.
52. Yan, J.-A.; Chou, M. Y. Oxidation Functional Groups on Graphene: Structural and Electronic Properties. *Phys. Rev. B: Condens. Matter Mater. Phys.* **2010**, *82*, 125403.
53. Wassmann, T.; Seitsonen, A. P.; Saitta, A. M.; Lazzeri, M.; Mauri, F. Clar's Theory, π-Electron Distribution, and Geometry of Graphene Nanoribbons. *J. Am. Chem. Soc.* **2010**, *132*, 3440–3451.
54. Kaloni, T. P.; Cheng, Y. C.; Faccio, R. Oxidation of Monovacancies in Graphene by Oxygen Molecules. *J. Mater. Chem.* **2011**, *21*, 18284–18288.

55. Lee, G.; Cho, K. Electronic Structures of Zigzag Graphene Nanoribbons with Edge Hydrogenation and Oxidation. *Phys. Rev. B: Condens. Matter Mater. Phys.* **2009**, *79*, 165440.
56. Tersoff, J.; Hamann, D. R. Theory and Application for the Scanning Tunneling Microscope. *Phys. Rev. Lett.* **1983**, *50*, 1998–2001.
57. Tersoff, J.; Hamann, D. R. Theory of the Scanning Tunneling Microscope. *Phys. Rev. B: Condens. Matter Mater. Phys.* **1985**, *31*, 805–813.
58. Hummers, W. S.; Offeman, R. E. Preparation of Graphite Oxide. *J. Am. Chem. Soc.* **1958**, *80*, 1339.
59. Fujii, S.; Enoki, T. Cutting of Oxidized Graphene into Nano-Sized Pieces. *J. Am. Chem. Soc.* **2010**, *132*, 10034–10041.
60. Vanderbilt, D. Soft Self-Consistent Pseudopotentials in a Generalized Eigenvalue Formalism. *Phys. Rev. B: Condens. Matter Mater. Phys.* **1990**, *41*, 7892–7895.
61. Giannozzi, P.; Baroni, S.; Bonini, N.; Calandra, M.; Car, R.; Cavazzoni, C.; Ceresoli, D.; Chiarotti, G. L.; Cococcioni, M.; Dabo, I.; *et al.* QUANTUM ESPRESSO: A Modular and Open-Source Software Project for Quantum Simulations of Materials. *J. Phys.: Condens. Matter* **2009**, *21*, 395502.
62. Monkhorst, H. J. Special Points for Brillouin-Zone Integrations. *Phys. Rev. B: Solid State* **1976**, *13*, 5188–5192.